remote sensing

MDPI

Article

Seasonal Characteristics of Disdrometer-Observed Raindrop Size Distributions and Their Applications on Radar Calibration and Erosion Mechanism in a Semi-Arid Area of China

Zongxu Xie [1,2], Hanbo Yang [1,2,*], Huafang Lv [1,2] and Qingfang Hu [3]

1 Department of Hydraulic Engineering, Tsinghua University, Beijing 100084, China; xie-zx19@mails.tsinghua.edu.cn (Z.X.); lvhf@tsinghua.edu.cn (H.L.)
2 State Key Laboratory of Hydro-Science and Engineering, Tsinghua University, Beijing 100084, China
3 State Key Laboratory of Hydro-Water Resources and Hydraulic Engineering, Nanjing Hydraulic Research Institute, Nanjing 210029, China; qfhu@nhri.cn
* Correspondence: yanghanbo@tsinghua.edu.cn

Received: 28 November 2019; Accepted: 10 January 2020; Published: 12 January 2020

check for updates

Abstract: Raindrop size distributions (DSDs) are the microphysical characteristics of raindrop spectra. Rainfall characterization is important to: (1) provide information on extreme rate, thus, it has an impact on rainfall related hazard; (2) provide data for indirect observation, model and forecast; (3) calibrate and validate the parameters in radar reflectivity-rainfall intensity (Z-R) relationships (quantitative estimate precipitation, QPE) and the mechanism of precipitation erosivity. In this study, the one-year datasets of raindrop spectra were measured by an OTT Parsivel-2 Disdrometer placed in Yulin, Shaanxi Province, China. At the same time, four TE525MM Gauges were also used in the same location to check the disdrometer-measured rainfall data. The theoretical formula of raindrop kinetic energy-rainfall intensity (KE-R) relationships was derived based on the DSDs to characterize the impact of precipitation characteristics and environmental conditions on KE-R relationships in semi-arid areas. In addition, seasonal rainfall intensity curves observed by the disdrometer of the area with application to erosion were characterized and estimated. The results showed that after quality control (QC), the frequencies of raindrop spectra data in different seasons varied, and rainfalls with R within 0.5–5 mm/h accounted for the largest proportion of rainfalls in each season. The parameters in Z-R relationships ($Z = \mathrm{a}R^{\mathrm{b}}$) were different for rainfall events of different seasons (a varies from 78.3–119.0, and b from 1.8–2.1), and the calculated KE-R relationships satisfied the form of power function KE = AR^{m}, in which A and m are parameters derived from rainfall shape factor μ. The sensitivity analysis of parameter A with μ demonstrated the applicability of the KE-R formula to different precipitation processes in the Yulin area.

Keywords: raindrop size distribution; radar reflectivity; raindrop spectrometer; semi-arid area

1. Introduction

Characteristics of precipitation show the impact of meteorological conditions [1], and the measurement of quantitative distribution of precipitation is important for studying the mechanism of global climate and environmental change [2]. Raindrop size distributions (DSDs) show the microphysical properties of a rainfall event and vary with precipitation both in time and space. The DSDs are of importance to enhance the accuracy of quantitative precipitation estimation (QPE) by weather radar, and raindrop spectra have been used to calculate radar reflectivity factors in many studies [3–6]. Thus, investigating the raindrop spectra is essential for providing information on the microphysical characteristics of different precipitation types, and improving the parameterizations of different rainfall processes.

Raindrop spectra can be measured by many methods, e.g., as done by Das et al., Waldvogel et al., Schönhuber et al. and Liu et al. [3,7–9], and these different methods vary in measurement principles and precision of data. In recent years, the raindrop disdrometer has been widely used to measure raindrop spectra because of its high measurement accuracy and small-time interval for data acquisition. Liu et al. [9] measured the precipitation in Nanjing, China and compared four different methods of rainfall to conclude that the disdrometer and other methods are consistent within the range of medium particle size. However, Zhang et al. [10] used three different methods to analyze the DSD characteristics in Zhuhai, China and found that the disdrometer had limitations in measuring small raindrops when compared to other methods. Raupach et al. [11] used a 2DVD device to correct the DSDs measured by three disdrometers and the correction showed its general applicability under different climate types. However, the study on the seasonal variation of rainfall characteristics in semi-arid areas of China using a raindrop disdrometer is very limited.

The measured raindrop spectra can be used to calibrate and validate the parameters in radar reflectivity-rainfall intensity (Z-R) relationships (quantitative estimate precipitation, QPE). Variability of DSDs in different forms of precipitation impact the radar reflectivity-rainfall intensity relationships (Z-R relationships, normally in the form of power function $Z = aR^b$, in which a and b are parameters derived from data fitting) [12,13], and the quantitative estimation of rainfall intensity (R) by Z-R relationships can be further modified. Sulochana et al. [14] investigated the Z-R relationships over a tropical station and concluded that the prefactor of Z-R relationships is larger for stratiform rain than for convective rain, which was in agreement with the results reported from two other tropical stations. Sulochana et al. also found that there were large variations in Z-R relationships in different seasons. Das et al. [3] analyzed the impact of different precipitation types on Z-R relationships in a hill station with a pronounced monsoon climate, and the results showed that the Z values of the shallow-convective system are the lowest, compared to other precipitation types. Das et al. concluded that the coefficient a is larger for stratiform rain than for convective and shallow-convective rain. However, there remains very limited research on using disdrometers to investigate raindrop spectra in semi-arid areas [15], and further research on the parameters in Z-R relationships is needed.

In addition, the measured raindrop spectra can be used to explore the mechanism of precipitation erosivity. The relationship between rainfall kinetic energy (KE) and intensity (R) is a significant approach to study the impact of precipitation on soil erosion [16], and a disdrometer can be deployed to measure the rainfall kinetic energy and intensity [17]. Angulo-Martínez et al. [18] measured and analyzed the uncertainty in KE-R relationships with five Parsivel disdrometers among three locations, and found that the types, accuracy and location of the disdrometers and precipitation types influence the estimation results of KE. Overestimation of the midsize raindrops led to a high estimation result of KE. Moreover, Carollo et al. [19] concluded that KE/R depends on the median volume diameter of precipitation events strictly, and this relationship does not rely on the locations of disdrometers. There have also been studies investigating the KE-R relationships in arid and semi-arid areas, e.g., Meshesha et al. and Abd Elbasit et al. [20,21], and many KE-R relationships were derived with this approach [22]. Nevertheless, many of the relationships vary greatly because of the different climate conditions, and a general formula for KE-R relationships needs to be derived to be suitably utilized in arid and semi-arid areas.

Yulin (in the northern region of Shaanxi Province, China) has a semi-arid climate, and the precipitation in this area is not evenly distributed throughout different seasons of the year [23]. The analysis of DSDs in different seasons is helpful to understand the variability of precipitation in this semi-arid area. The objectives of this paper are: (1) to analyze the detailed statistical data of DSDs based on the observation of a raindrop disdrometer located in Yulin, and collect data on the variability of microphysical characteristics of precipitation in different seasons; (2) to investigate the Z-R relationships in different seasons, and analyze the variability of the parameters in the Z-R relationships across different precipitation types; (3) to derive a theoretical formula for KE-R relationships and further analyze the calculated results.

The following sections are organized below. Section 2 describes the research method, the datasets of the research area, and the derivation processes of theoretical formula. Section 3 analyzes the observed results statistically and presents the comparison of different precipitation periods in different seasons. Section 4 presents a further discussion of the comparison of disdrometer- and gauges-measured rainfall data, the comparison of different Z-R relationships and the theoretical formula of KE-R relationships through sensitivity analysis. Section 5 gives the conclusion.

2. Materials and Methods

2.1. Observation Station and Disdrometer Datasets

Microphysical characteristics of different precipitation types were measured at Yulin Ecohydrological Station (109°28′2.7′′E, 38°26′43.6′′N, 1236 m above sea level (a.s.l.), located in Mu Us Sandy Land) in Shaanxi Province, China. Mu Us Sandy Land has a semi-arid climate type with a low amount of precipitation [24]. The average annual precipitation in this area is 413 mm (from the year 1951 to 2018, measured by Yulin Meteorological Station (109°28′12′′E, 38°9′36′′N, 936 m a.s.l.)).

Figure 1a shows the location of Yulin Ecohydrological Station and Yulin Meteorological Station. One OTT Parsivel-2 Disdrometer was placed in Yulin Ecohydrological Station, and continuously recorded data during a 1-year period between 10 August 2018 and 10 August 2019. There are also four TE525MM rainfall gauges placed at the same location (shown in Figure 1b), and the specific placement of the disdrometer and the four gauges is proposed by Xie et al. [25], providing a reference for the measurement data by the disdrometer. Data were recorded every 30 min during the researching period, with the four gauges recording data simultaneously and individually. The disdrometer conducted a 54 cm^2 laser beam to record the rainfall spectrum every 1 min. The record of the disdrometer includes two parts: raindrop diameters (D) and raindrop terminal velocity (v). When precipitation particles pass the laser beam of the sensor, the beam is blocked off by the particles equal to the diameters, and the output voltage will be reduced. If there is no particle passing through, the voltage will then be recorded as maximum. The duration of the reducing signal will be used to determine the terminal speed of a particle. Through the observation by the disdrometer, radar reflectivity (Z), rainfall intensity (R) and kinetic energy (KE) are derived from D and v. Figure 2 summarizes how the materials and methods and results are managed via a schematic.

2.2. Processing Microphysical Datasets from Disdrometer

In order to process the calculation of the characteristic variables of precipitation, the formulas are derived as follows:

$$\mathrm{N}(D_i) = \sum_{j=1}^{32} \frac{n_{ij}}{V_j \cdot \Delta D_i} = \sum_{j=1}^{32} \frac{n_{ij}}{A \cdot \Delta t \cdot v_j \cdot \Delta D_i} \tag{1}$$

where $\mathrm{N}(D_i)$ (mm^{-1} · m^{-3}) is the number concentration of raindrops per unit diameter interval for raindrops per unit volume with the diameter equal to D_i (the ith-bin of diameters of the spectra); $A = 5.4 \times 10^{-4}$ m^2 is the sampling area scanned by the laser beam; Δt = 60 s is the sampling time interval; v_j is the raindrop terminal velocity of the jth-bin of velocities of the spectra; ΔD_i is the class spread of the ith-bin of diameters of the spectra.

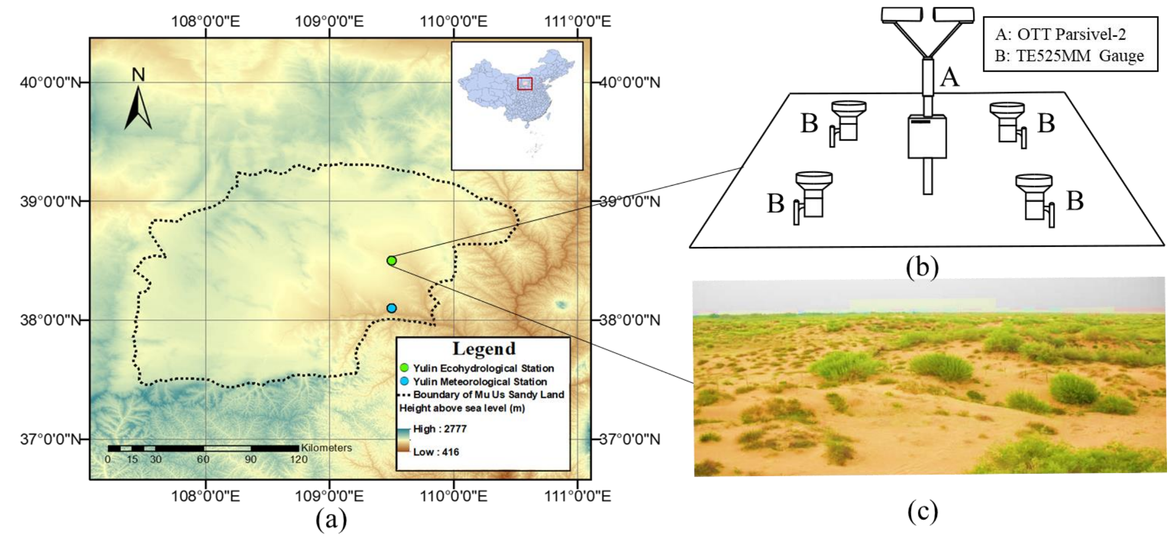

Figure 1. (**a**) The location of Yulin Ecohydrological Station (green point) and the location of Yulin Meteorological Station (blue point) and the DEM (Digital Elevation Model) characteristics around the sites. The red rectangle in the China map highlights the location of Mu Us Sandy Land; (**b**) the OTT Parsivel-2 disdrometer and the surrounding 4 TE525MM rain gauges in Yulin Ecohydrological Station; (**c**) vegetation cover situation in Yulin Ecohydrological Station.

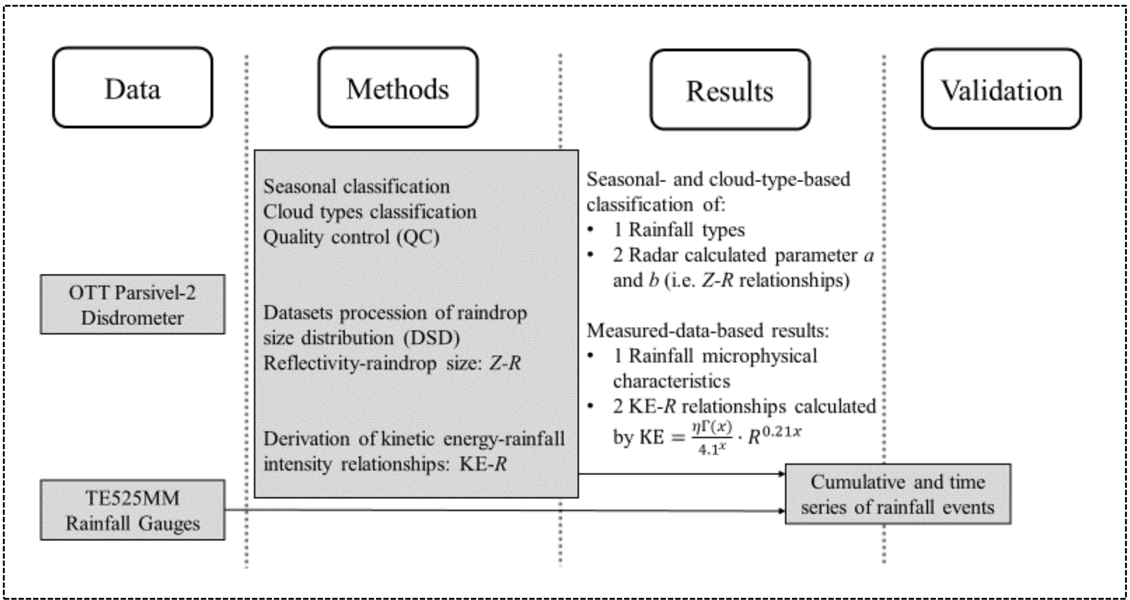

Figure 2. Schematic of the research technical route in this study.

The nth-moment of the DSD can be calculated as:

$$M_n = \int_0^\infty D^n N(D) dD \tag{2}$$

Moreover the 6th-moment of the DSD is equal to the radar reflectivity Z (mm^6·m^{-3}):

$$Z = M_6 = \int_0^\infty D^6 N(D) dD = \sum_{i=3}^{32} D_i^6 N(D_i) \Delta D_i \tag{3}$$

where the 1st-bin and the 2nd-bin of diameters are not evaluated in the measurements of the OTT Parsivel-2 because these two bins are out of the measurement range of the disdrometer, thus i starts from 3 to 32.

The $R_{\text{total(i,j)}}$ $(\text{mm}\cdot\text{h}^{-1})$ is the total rainfall per unit time in the n_{ij} grid:

$$R_{\text{total(i,j)}} = v_j \cdot N(D_i) \cdot \Delta D_i \cdot \frac{1}{6}\pi D_i^3 \cdot 3600 \cdot 10^{-6} = \frac{3\pi}{5000} v_j D_i^3 N(D_i) \Delta D_i \tag{4}$$

The rainfall intensity R $(\text{mm}\cdot\text{h}^{-1})$ is the summation of $R_{\text{total(i,j)}}$, and thus, can be calculated as:

$$R = \frac{3\pi}{5000} \sum_{i=3}^{32} \left(\sum_{j=1}^{32} v_j D_i^3 N(D_i) \Delta D_i \right) \tag{5}$$

The content of liquid raindrop W $(\text{g}\cdot\text{m}^{-3})$ is the mass of liquid raindrops per unit volume:

$$W = \frac{\pi}{6} \cdot 10^{-3} \cdot \int_0^\infty D^3 N(D) dD = \frac{\pi}{6} \cdot 10^{-3} \cdot \sum_{i=3}^{32} D_i^3 N(D_i) \Delta D_i \tag{6}$$

The gamma distribution of raindrop spectra is derived as:

$$N(D) = N_0 D^\mu \exp(-\Lambda D) \tag{7}$$

where N_0 $(\text{mm}^{-1-\mu} \cdot \text{m}^{-3})$ is the intercept parameter and varies in dozens of orders of magnitudes [26]. Thus, the normalized intercept parameter Nw $(\text{mm}^{-1} \cdot \text{m}^{-3})$ is used by Testud et al. [27] to represent N_0, in order for the characteristics of the parameter of distribution of raindrop spectra can be calculated without any assumption about the DSD shapes:

$$N_w = \frac{4^4 M_3^5}{6 \rho_w M_4^4} \tag{8}$$

N_w is better than N_0 for representing the raindrop concentration with certain raindrop sizes, as is not dependent on parameter μ. The mass-weighted mean diameter Dm(mm), and the rainfall shape parameter μ (dimensionless, related to rainfall types [28]), can be expressed as [29,30]:

$$Dm = \frac{4+\mu}{\Lambda} \tag{9}$$

$$\mu = \frac{1}{2\left(1 - \frac{M_4^3}{M_3^2 M_6}\right)} \left\{ 11 \frac{M_4^3}{M_3^2 M_6} + \left[\frac{M_4^3}{M_3^2 M_6} \left(\frac{M_4^3}{M_3^2 M_6} + 8 \right) \right]^{\frac{1}{2}} - 8 \right\} \tag{10}$$

The slope parameter of gamma distribution Λ (mm^{-1}) is dependent on parameter μ, and Seela et al. [31] concluded that μ-Λ relationships vary with different precipitation types in different areas. In this study, the Λ is expressed as a function of the 2nd and 4th-moment of the DSD and parameter μ [32]:

$$\Lambda = \left[\frac{M_2 \Gamma(\mu+5)}{M_4 \Gamma(\mu+3)} \right]^{\frac{1}{2}} \tag{11}$$

2.3. Precipitation Types and Quality Control (QC)

In this study, in order to analyze the characteristics of raindrop spectra in different precipitation types, the precipitation data is classified into convective and stratiform rain based on the rainfall intensity [14]. Quality control is carried out in this study because there are errors in the measurement of large diameters of raindrops using the disdrometer. In this study, raindrops larger than 6 mm in diameter were considered to have crushed during falling [33]. Therefore, raindrops larger than 6 mm in diameter are excluded in this study

Figure 3 illustrates the principle of classifying stratiform, convective, mixed-cloud rain and non-rainfall events. In this study, the effective observation range of raindrop diameter is 0.25–6 mm. Raindrop spectrum data with the total number of raindrops less than 10 or rain intensity less than 0.5 mm/h is regarded as noise [34,35].

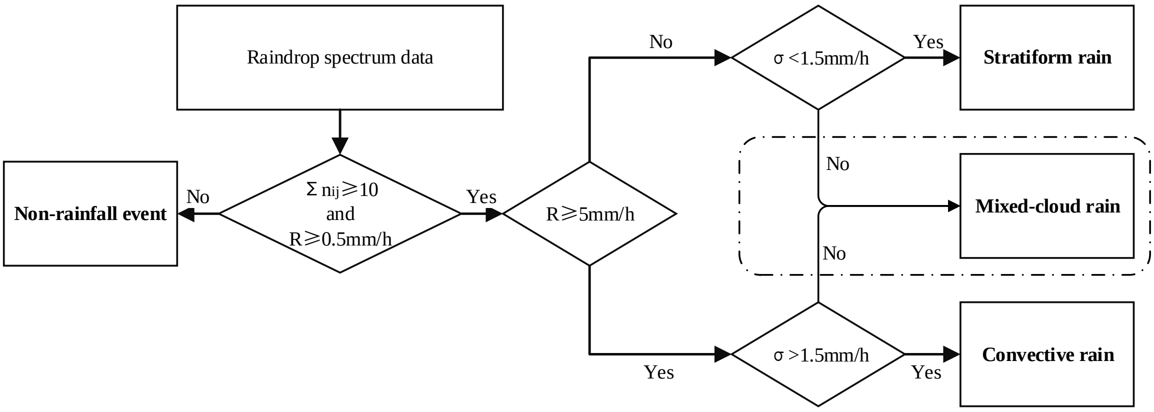

Figure 3. Classifying stratiform, convective rain and non-rainfall events. This classification method is derived by Li et al. [36] and used in Mt. Huangshan (118°10′E, 30°07′N, 1351 m a.s.l.), and is considered valid in this study to classify stratiform/convective rain.

The quality control principle is similar to the method used by Li et al. [36]. For an instantaneous moment t_n during a rainfall event, if the rain intensity R within the time range $[t_n - N_s,\ t_n + N_s]$ is > 5 mm/h and the standard deviation is >1.5 mm/h, the event is classified as a convective rainfall event; if the rain intensity R within the time range $[t_n - N_s,\ t_n + N_s]$ satisfies 0.5 < R < 5 mm/h and the standard deviation is <1.5 mm/h, then the event is classified as a stratiform rainfall event. Other rainfall events are classified as mixed-cloud rain [37].

2.4. Derivation of KE-R Relationships

Rainfall kinetic energy (KE) can be calculated from the raindrop disdrometer, rainfall terminal velocity and raindrop size distribution. The total kinetic energy KE (J/(m^3·s)) can be derived as [25,38]:

$$\mathrm{KE} = \frac{1}{12}\rho\pi a^3 N_0 \int_0^\infty D^{\mu+3+3b} e^{-\Lambda D} dD \tag{12}$$

where a = 3.78 and b = 0.67 are constant parameters [39]. In arid or semi-arid areas, most of the precipitation is of weak or moderate levels and Marshall et al. [40] concluded that N_0 in the expression of $N(D)$ is almost fixed to 0.08 cm^{-4}. The parameter x is defined as:

$$x = \mu + 4 + 3b = \mu + 6.01 \tag{13}$$

From Equations (12) and (13), the KE can be further expressed as:

$$\mathrm{KE} = \frac{\rho\pi a^3 N_0}{12\Lambda^x} \int_0^\infty t^{x-1} e^{-t} dt = \frac{\rho\pi a^3 N_0 \Gamma(x)}{12\Lambda^x} \tag{14}$$

The expression of Λ is:

$$\Lambda = 4.1R^{-0.21} \tag{15}$$

which is commonly used in the calculation of KE-R relationships in many studies [41–43], and:

$$\mathrm{KE} = \frac{\rho \pi a^3 N_0 \Gamma(x)}{12 \cdot 4.1^x} \cdot R^{0.21x} \tag{16}$$

The parameter η is defined as:

$$\eta = \frac{\rho \pi a^3 N_0}{12} \tag{17}$$

and is constant. Then:

$$\mathrm{KE} = \frac{\eta \Gamma(x)}{4.1^x} \cdot R^{0.21x} \tag{18}$$

Therefore, the empirical formula of the relationship between KE and R with the variable parameter x for the semi-arid area is derived.

3. Results

3.1. Data after Quality Control

In this study, 8184 records are selected as rainfall events, including 7388 stratiform and 796 convective data. The amount of observed mixed-cloud rain is zero. Figure 4 shows the frequency accumulation curve of rainfall intensity recorded. The average $\overline{R}$ of the recorded data is 2.3 mm/h (the calculated average $\overline{R}$ includes only rainy hours, as shown in Section 2.3), and the data with rainfall intensity less than 5 mm/h is more than 90% of the total time of rainfall data.

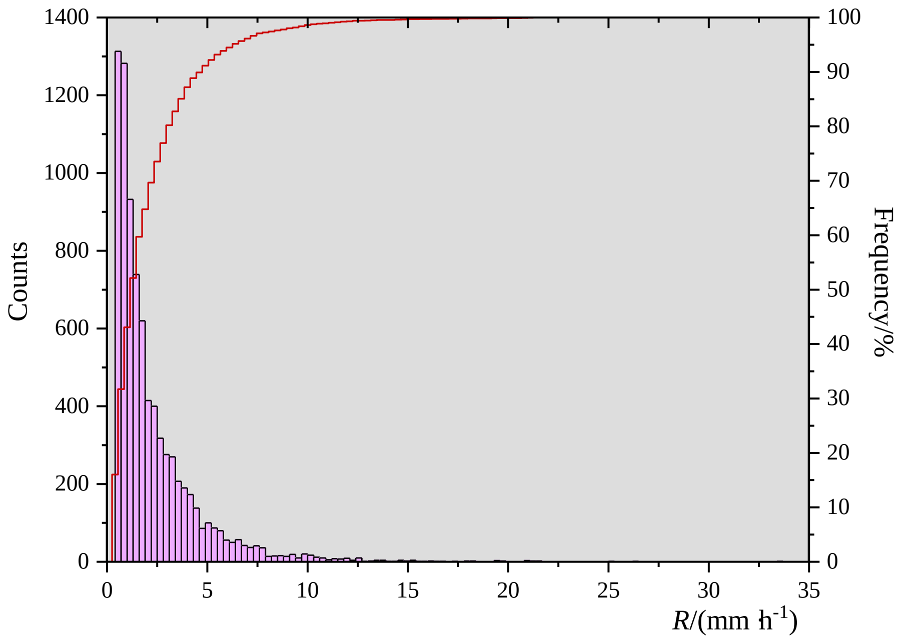

Figure 4. Frequency distribution of rain rates calculated from the whole OTT Parsivel-2 disdrometer datasets.

A division of the rainfall data into different seasons (spring from March to May, Summer from June to August, Autumn from September to November and Winter from December to February) and rainfall types (stratiform and convective rain) acquired by the OTT Parsivel-2 is reported in Table 1. The results shown in Table 1 reflect the trend of precipitation change in this region with different seasons. The frequency of raindrop spectra data recorded in summer is the highest (with 7019 records), followed by autumn (4230 records), spring (3387 records) and winter (only 116 records). In spring, summer and autumn, the total time of stratiform rainfall events T_s is higher than the total time of convective rainfall events T_c, which reflects the precipitation characteristics of semi-arid areas [44].

The percentage of stratiform rain is from small to large summer (85.9%), spring (93.5%) and autumn (95.5%). Winter is not considered when comparing the characteristics of different seasons due to too few liquid precipitation data recorded. The percentage of convective rain, ordered from small to large, is spring (4.5%), autumn (6.5%) and summer (14.1%). In summer the R varies most and has the highest standard deviation of 2.8 mm/h. However, the percentage of rainfall time over the seasons is ordered from small to large, are spring (1.4%), autumn (1.7%) and summer (3.0%).

Table 1. Disdrometer-measured data of different seasons: total time with recorded data, the percentage of stratiform and convective rain and percentage of different ranges of rainfall intensity; maximum and average rainfall intensity, and standard deviation of rainfall intensity.

Rainfall Characteristics	Spring (March–May)	Summer (June–August)	Autumn (September–November)	Winter (December–February)
Total time with data recorded T_{total} (min)	3387	7019	4230	116
Total time of stratiform rain T_s (min)	1813	3431	2126	18
Total time of convective rain T_c (min)	86	563	147	-
Percentage of stratiform rain $T_s/(T_s+T_C)$ (%)	95.5	85.9	93.5	100
Percentage of convective rain $T_c/(T_s+T_c)$ (%)	4.5	14.1	6.5	-
Percentage of rainfall time over the season (%)	1.4	3.0	1.7	≈0
Maximum rainfall intensity R_{max} (mm·h^{-1})	12.6	33.7	21.2	1.1
Average $\overline{R}$ (mm·h^{-1})	2.0	2.6	2.0	0.7
Median R_m (mm·h^{-1})	1.9	1.9	1.6	0.7
Precipitation Accumulation P_{total} (mm)	76.7	236.9	105.9	- *
Standard deviation of rainfall intensity R (mm·h^{-1})	1.6	2.8	1.8	0.15
$T_{0.5\text{–}2\ \mathrm{mm \cdot h^{-1}}}/(T_s+T_C)$ (%)	60.3	58.8	66.4	100
$T_{2\text{–}5\ \mathrm{mm \cdot h^{-1}}}/(T_s+T_C)$ (%)	35.1	27.1	27.1	-
$T_{5\text{–}10\ \mathrm{mm \cdot h^{-1}}}/(T_s+T_C)$ (%)	4.2	11.3	6.0	-
$T_{>10\ \mathrm{mm \cdot h^{-1}}}/(T_s+T_C)$ (%)	0.4	2.8	0.5	-

* The rainfall accumulation is not calculated in winter because of the inclusion of solid precipitation (e.g., snow).

Weak and moderate rainfalls (with rainfall intensity satisfying $0.5 < R < 5$ mm/h) account for the largest proportion of rainfalls in each season, and data satisfying $R > 5$ mm/h in summer is of the highest percentage of total rainfall time in the season (11.3%). The R_{max} is 33.7 mm/h in summer, 21.2 mm/h in autumn and 12.6 mm/h in spring. The $\overline{R}$ and P_{total} in summer are also the highest (2.6 mm/h and 236.9 mm, respectively), while the difference in $\overline{R}$ between spring (2.0 mm/h) and autumn (2.0 mm/h) is not significant. The difference in R_m between spring (1.9 mm/h) and summer (1.9 mm/h) is not significant.

3.2. Microphysical Characteristics of Precipitation in Different Seasons

Figure 5 is the distribution of different diameters with varying velocities obtained in different seasons. In spring, summer and autumn, the majority of raindrop particles are in an area close to the theoretical curve proposed by Beard [45]; in winter, the data is accumulated in low levels of both v and D. Data are overall lying over the theoretical curve in spring, summer and autumn; in winter, however, the velocities are underestimated compared to the theoretical curve in winter. This is because the type of rainfalls during winter was mainly snow (regarded as solid rainfalls) and could cause deviation in call speed, and the raindrop data with D > 6 mm are excluded as shown in Section 2.3.

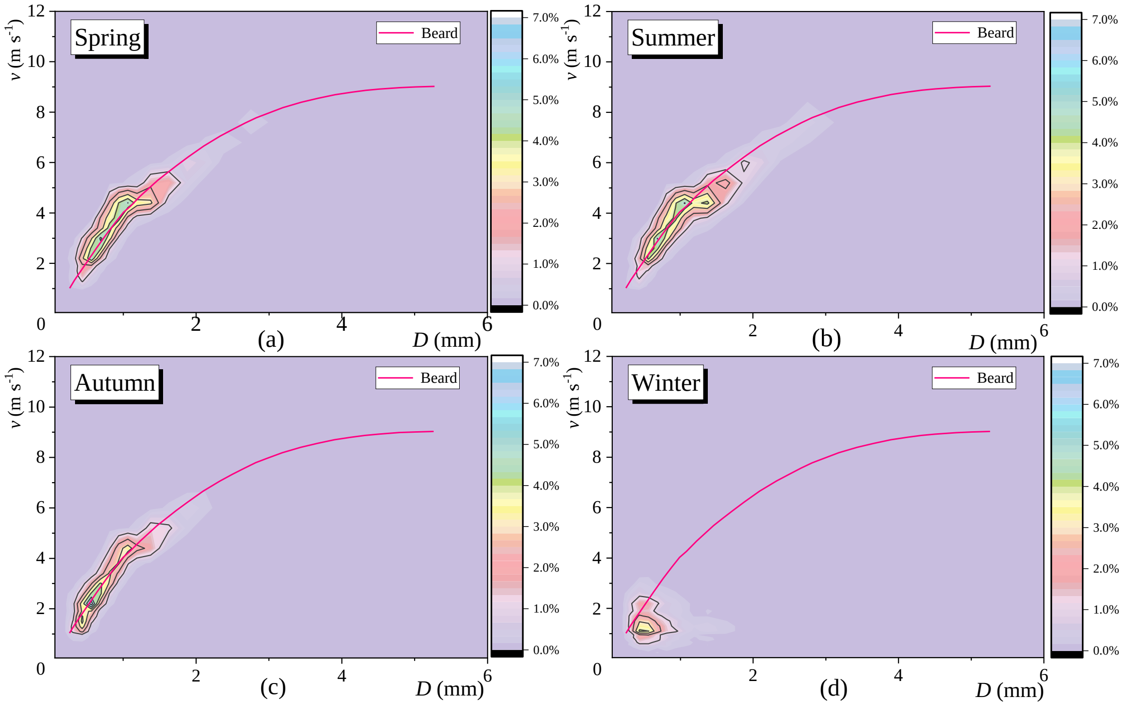

Figure 5. Plots of measured raindrop terminal velocity-diameter relationships in different seasons. The red curve is derived by Beard [45] in 1976, giving the relationships between v and D, and used as the reference line for the v-D distribution in each season (**a**) spring; (**b**) summer; (**c**) autumn; (**d**) winter.

Figure 6 shows the histogram of Dm and $\log_{10}Nw$ in different seasons and precipitation types. The yearly average Dm and $\log_{10}Nw$ are 1.41 and 3.91 mm, respectively. The average Dm of stratiform (convective) rain from small to large is 1.38 mm (1.46 mm) in summer, 1.46 mm (1.52 mm) in spring and 1.51 mm (1.57 mm) in autumn. However, there is less variation in average $\log_{10}Nw$ data among the three seasons. The average $\log_{10}Nw$ of stratiform rain from small to large is 3.88 mm in summer, 3.89 mm in autumn and 3.92 in spring. However, the maximum of the average $\log_{10}Nw$ of convective rain is 4.28 in summer. This reflects the micro-physical characteristics of rainfall in Yulin area: according to the results shown in Section 3.1, the average rainfall intensity is larger in summer than in spring and autumn. According to Equation (5), the rain intensity is related to raindrop diameter and DSD. The average Dm of different precipitation types in different seasons shows that for stratiform rain, R is affected more by the raindrop diameter; for convective rain, R is affected more by DSD. The average value of Dm is slightly less than that of in southern China (1.46 mm) [10].

Besides the average value, standard deviation and skewness of different Dm and $\log_{10}Nw$ were also calculated. The standard deviation of Dm in stratiform and convective rain among different seasons varies from 0.19 mm to 0.26 mm. The skewness of Dm and Nw in stratiform and convective rain are less than 0 in spring and autumn, illustrating the frequency of the data below the Dm_{mean} (Nw_{mean}) is less than data above the Dm_{mean} (Nw_{mean}). However, the skewness of Dm and Nw in stratiform and convective rain in summer are larger than 0, illustrating the frequency of the data below the Dm_{mean} (Nw_{mean}) is more than data above the Dm_{mean} (Nw_{mean}).

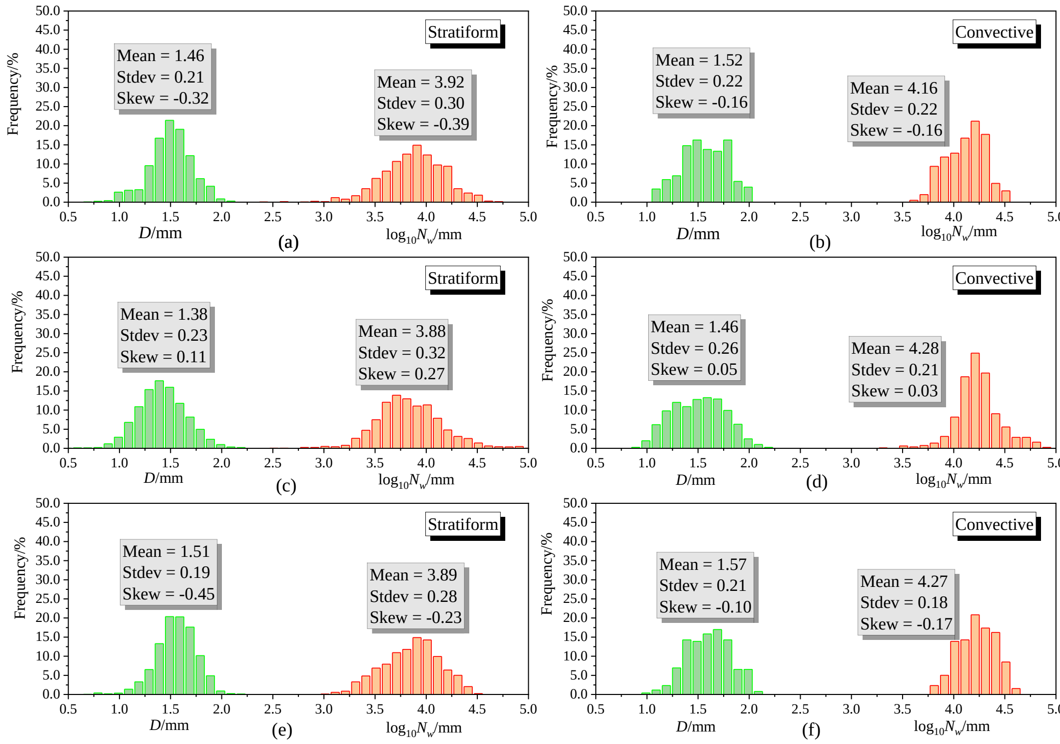

Figure 6. Frequency histogram of mass-weighted median diameter *Dm* and the denary logarithm of *Nw* in different precipitation types and different seasons calculated from the data measured by OTT Parsivel-2. (**a**) Histogram in stratiform rain in spring; (**b**) Histogram in convective rain in spring; (**c**) Histogram in stratiform rain in summer; (**d**) Histogram in convective rain in summer; (**e**) Histogram in stratiform rain in autumn; (**f**) Histogram in convective rain in autumn. The average value, standard deviation and skewness are also given for *Dm* and *Nw* in each plot.

Figure 7 shows the *Nw*-*R* relationships in different seasons and precipitation types. The base-10 logarithm of *Nw* is used to fit the relationship curves $\log_{10}Nw = cR^{d}$, in which c and d are parameters fitted by measured data. For the error bars in each panel, *R* in the range (0.5, 5) (for stratiform rain) are divided into nine intervals evenly, and in the range (5, 35) (for convective rain) are divided into five intervals ($5 < R < 10$, $10 < R < 15$, $15 < R < 20$, $20 < R < 25$ and $R > 25$ mm·h^{-1}), and error bars are used for each interval. The error bars for each interval are based on the mean value of *R* and log10*Nw*, with the ±1 Stdev (standard deviation), respectively. A significance analysis of fitting results is also proposed [46]. The p-values in each panel of Figure 7 are derived from the fitting tests of the power function. The p-values show that the fits for stratiform rain are statistically relevant and sound (shown in Figure 7a,c,e). When comparing the disparity in precipitation types, parameters c and d have a smaller range in variability in different seasons. Figure 7a,c,e indicate that for stratiform rain, the difference of parameter c among different seasons ranges in 3.73–3.79 ($p < 0.05$). However, the parameter c for convective rain varies in a larger range of 3.86–4.14 ($p < 0.1$). For each season, the parameter a of stratiform rain is smaller than that of convective rain. The difference in parameter d is small among different seasons, and the d of stratiform rain is larger than that of convective rain.

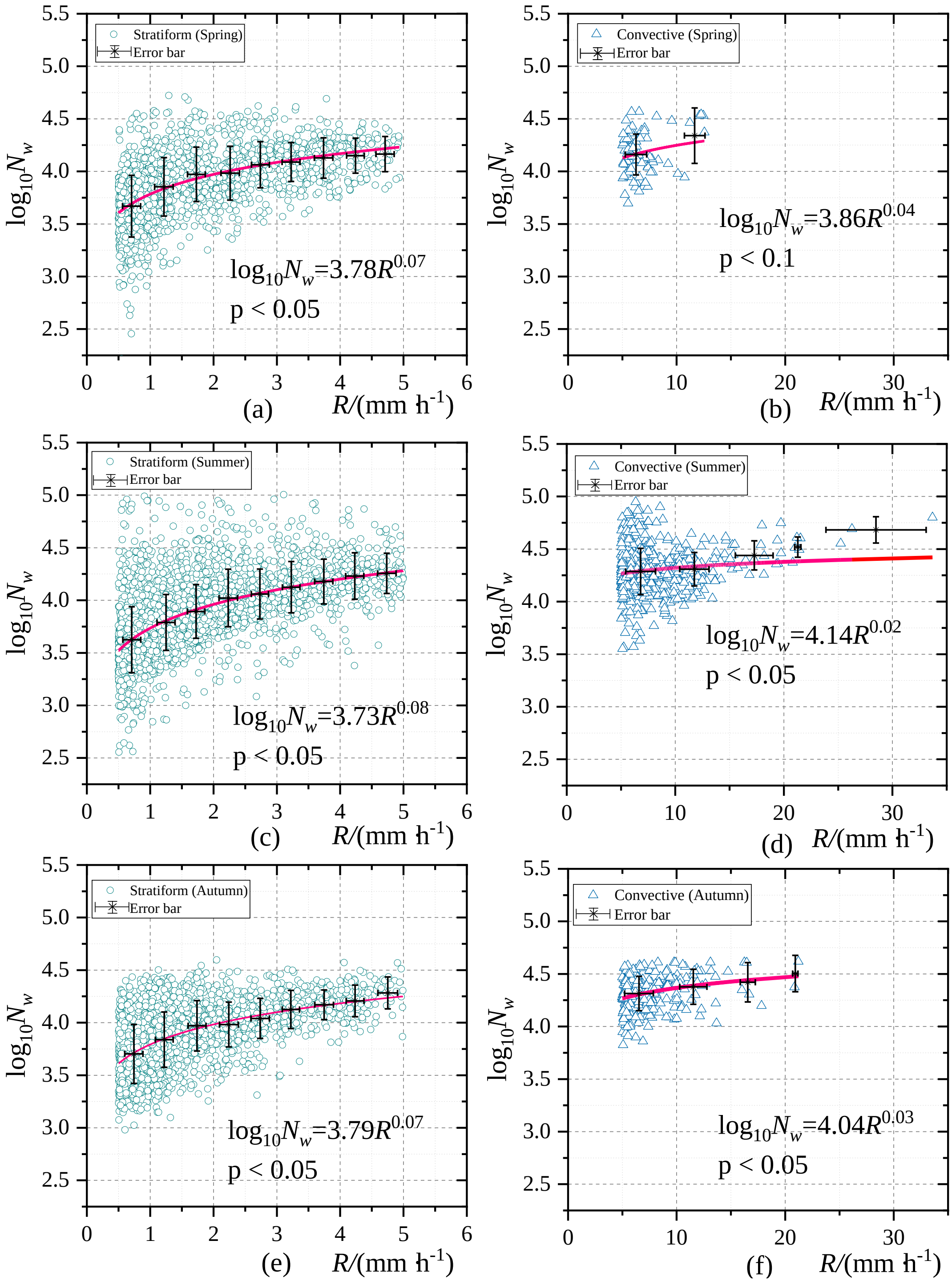

Figure 7. *Nw-R* relationships for different precipitation types in different seasons. The fitted power formula based on the least-squares method is also shown in each plot: (**a**) stratiform rain in spring; (**b**) convective rain in spring; (**c**) stratiform rain in summer; (**d**) convective rain in summer; (**e**) stratiform rain in autumn (**f**) convective rain in autumn.

3.3. Z-R Relationships in Different Rainfall Events

Three rainfall events were selected to illustrate the differences between the data measured by OTT Parsivel-2 Disdrometer and four TE525MM Rainfall Gauges. The three events are, respectively, chosen from each season, regarding their representation of different levels of rainfall intensity (all of the three events last for > 4h and include stratiform and convective records).

Table 2 shows the precipitation characteristics of these rainfall events. S/C records show the relative rates of amounts of the stratiform and the convective records during the selected rainfall events, for which Event 1, 2 and 3 are 662%, 888% and 753%, respectively. The results correspond to the average rainfall intensity $\overline{R}$ of each rainfall event. Event 2 is with the least $\overline{R}$ (2.42 mm·h^{-1}), while Event 1 is with the highest $\overline{R}$ (3.07 mm·h^{-1}).

Table 2. Precipitation characteristics of selected three rainfall events.

Rainfall Number	Rainfall Time	Season	$\overline{R_d}$/(mm·h^{-1}) *	$\overline{R_g}$/(mm·h^{-1}) **	Duration	S/C Records
Event 1	19–20 April 2019	Spring	3.36	3.51	4 h 30 min	225/34
Event 2	3 August 2019	Summer	1.65	1.78	12 h 30 min	897/101
Event 3	1 September 2018	Autumn	3.09	3.22	4 h	241/32

* Derived from disdrometer-measured raindrop spectra. See in Equation (5). ** Obtained by the four rainfall gauges and averaged.

Figure 8 shows the difference in Z-R relationships of the three rainfall events of spring, summer and autumn, and the results are $Z = 109.6R^{2.1}$ (Event 1), $Z = 119.0R^{1.8}$ (Event 2) and $Z = 78.3R^{1.9}$ (Event 3). The parameter a of each of the three rainfall events is less than the parameter a of the default Z-R relationship [47] ($Z = 300R^{1.4}$, where parameter a is equal to 300). Parameter b in $Z = \mathrm{a}R^{\mathrm{b}}$ has only slight difference among different rainfall events, and ranges in 1.8–2.1 ($p < 0.05$). This is consistent with previous studies [48–51], that parameter b in $Z = \mathrm{a}R^{\mathrm{b}}$ varies in the range of 1–2.87 ($p < 0.05$). The raindrop spectra have obvious changes for different precipitation types, causing the parameters of Z-R relationships to vary. It is clear that the Z-R relationships of rainfall events vary depending on the season and the precipitation types. The rainfall events with a higher S/C rate tend to have a higher average rainfall intensity. Therefore, precipitation estimates for different types should be treated as such. The results indicate that there is a need to utilize modified Z-R relationships in different seasons when calculating the rainfall intensity by the QPE method.

3.4. KE-R Relationships

The rainfall kinetic energy KE and rainfall intensity R are calculated based on Equations (5) and (18), respectively. The KE-R relationships of stratiform rain in different seasons are derived in the form of a power function. The fitting results show the KE-R relationships satisfy the form of power function $\mathrm{KE} = AR^{\mathrm{m}}$, in which A and m are parameters.

Figure 9 shows that the stronger the rainfall intensity is, the faster the rainfall kinetic energy tends to increase. The exponent of different power functions m varies from 1.45 to 1.82, in order from small to large, spring < autumn < summer. Parameter A has similar values in spring (equal to 8.56) and in summer (equal to 8.10), but in autumn the parameter A is 5.56. The value of the parameter A is closely related to the raindrop spectra [52]. The parameter A is also related to the median rainfall intensity R_{m}, which results in the decrease of A in autumn compared to spring and summer.

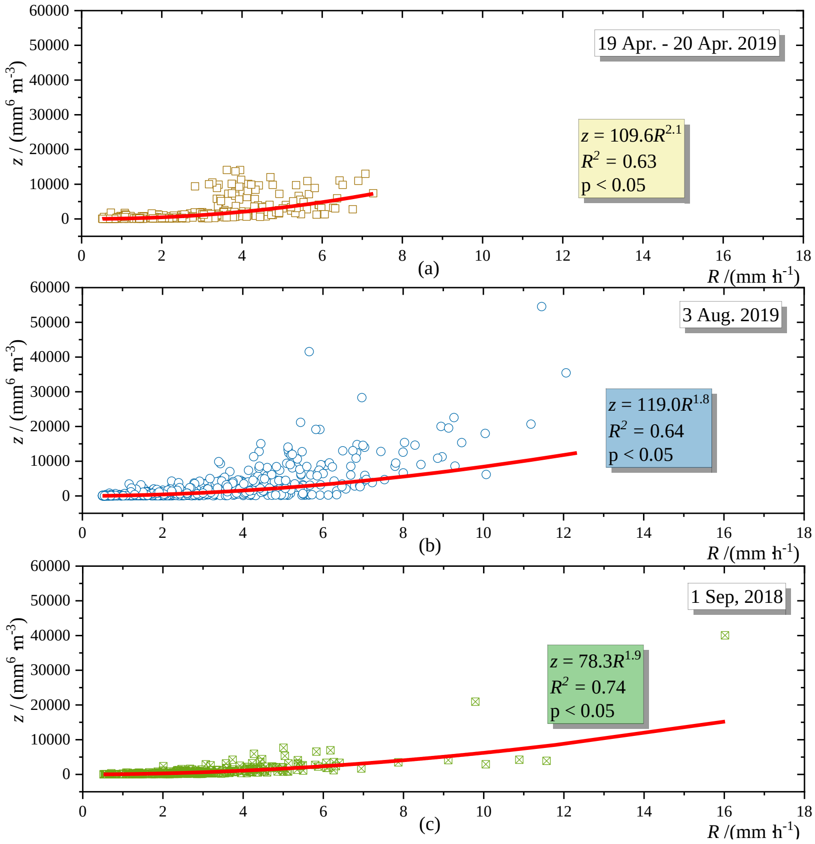

Figure 8. *Z*-*R* relationships ($Z = aR^b$) in three rainfall events. Each rainfall event is selected from different seasons (spring, summer and autumn). (**a**) *Z*-*R* relationship of a rainfall event in spring, from 19 April to 20 April 2019; (**b**) *Z*-*R* relationship of a rainfall event in summer, on 3 August 2019; (**c**) *Z*-*R* relationship of a rainfall event in autumn, on 1 September 2018; the fitted curves are derived based on the power function, which are solid red curves in (**a**–**c**).

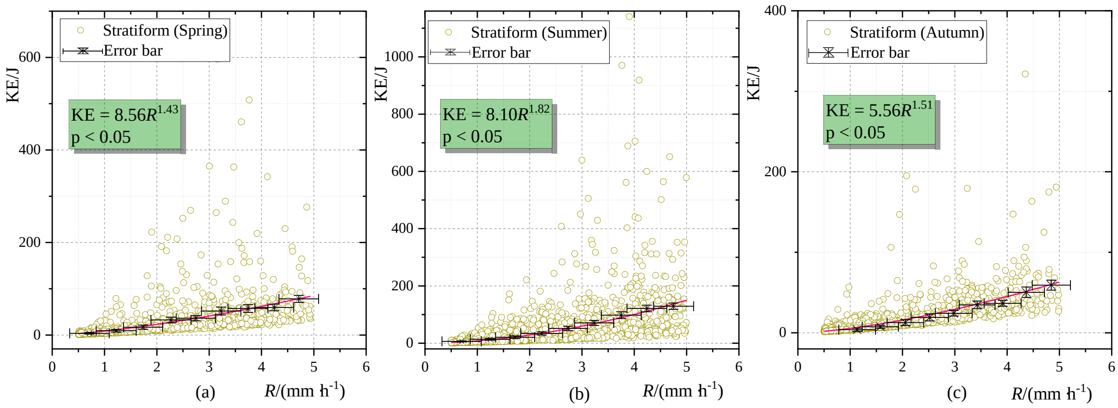

Figure 9. KE-*R* curves fitted in different seasons. Data of stratiform rain in spring, summer, and autumn are analyzed. (**a**) KE-*R* relationship in spring; (**b**) KE-*R* relationship in summer; (**c**) KE-*R* relationship in autumn. For the error bars in each panel, *R* in the range (0.5, 5) are divided into nine intervals evenly, and error bars are used for each interval. The error bars for each interval are based on the mean value of *R* and KE, with the ±1 Stdev (standard deviation), respectively.

4. Discussion

4.1. Uncertainty Analysis of Disdrometer-Measured Data

Figure 10 shows the relationship between two different measurements on a daily scale. Each point represents the total rainfall of a given day during the 1-year observation period. The abscissa is the total measured rainfall of Parsivel-2, and the ordinate is the averaged total rainfall measured by four TE525MM Gauges (data with both daily total rainfall greater than 1mm are taken for analysis). The results show that the disdrometer-measured data demonstrates a good correlation with the average rainfall gauge-measured data, and the deviation is mainly caused by the instrument theoretical error in measurement of disdrometer and gauges (e.g., sampling error), which was concluded by Tokay et al. [29]. The measured rainfall data of the disdrometer is suitable for this semi-arid area.

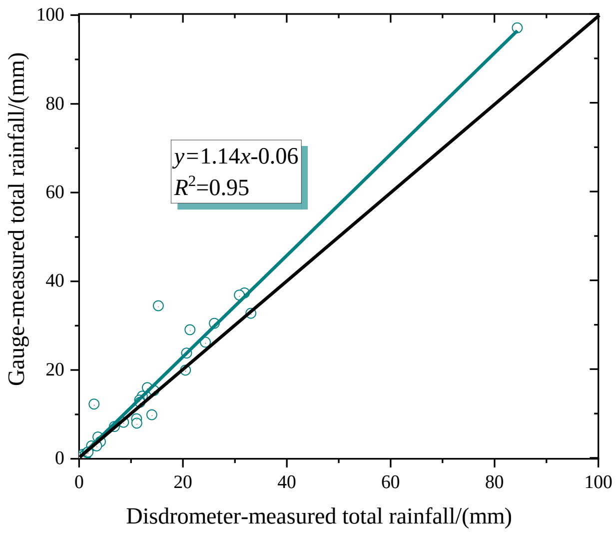

Figure 10. Scatter plot of gauge- and disdrometer-measured total rainfall on a daily scale. The results obtained by the two measurement methods are compared with the scatter plot. The solid green line is the fitted result.

Figure 11 shows the precipitation process of three rainfall events, with the calculated average of the data measured by four rainfall gauges. The determinate coefficient R^2 of a linear relationship between Parsivel Disdrometer and TE525MM Gauges is 0.68 for (a), 0.83 for (b) and 0.96 for (c). The standard deviations of disdrometer-measured (gauge-measured) rainfall intensity in (a), (b) and (c) are 1.37 mm/h (2.90 mm/h), 1.02 mm/h (1.43 mm/h) and 1.43 mm/h (2.46 mm/h), respectively. The standard deviation of the disdrometer-measured data in each season is less than the gauge-measured data in the corresponding season. In order to further compare the difference between disdrometer-measured and gauges-measured data, the mean absolute error(MAE) and the root mean square error(RMSE) of the events are also given. Event 3 has the smallest MAE (0.69 mm·h^{-1}) and smallest RMSE (0.99 mm·h^{-1}) among the three events. This indicates that the disdrometer can potentially estimate the precipitation with better performance during Event 3, according to the comparison with gauge-measured data.

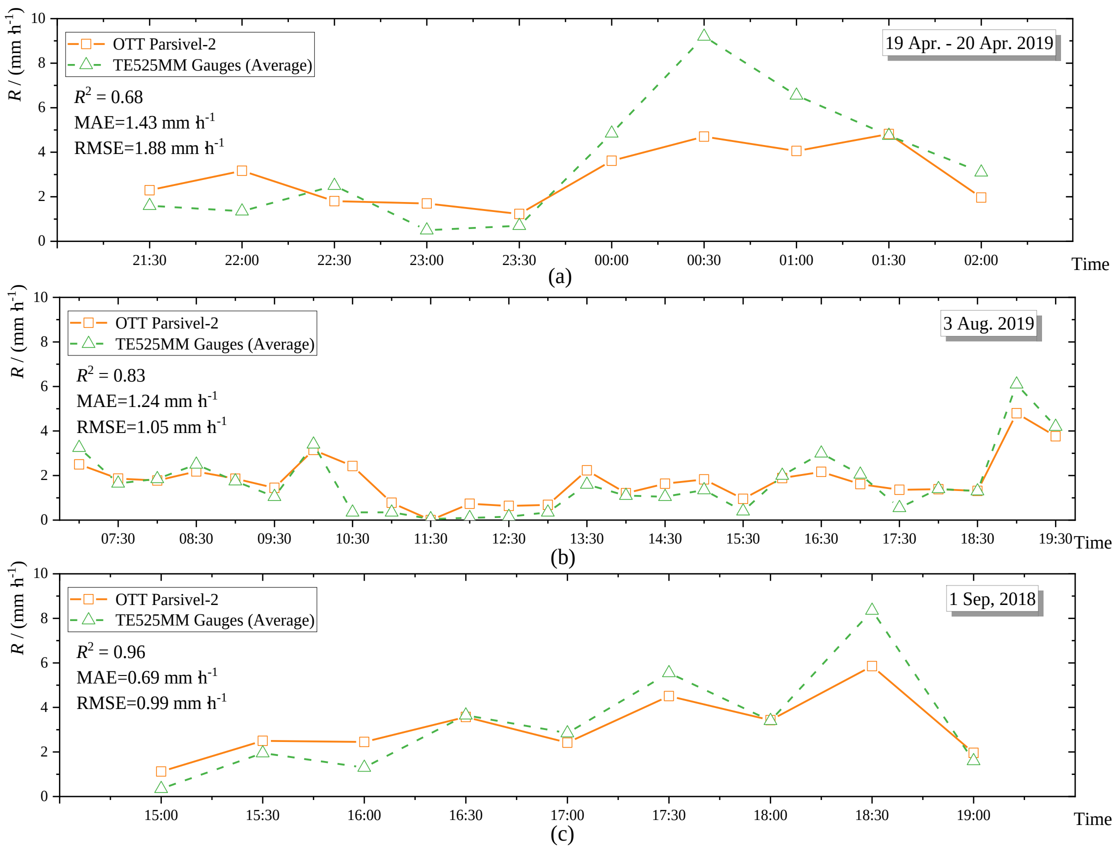

Figure 11. The comparison of measurement results of OTT Parsivel-2 (orange solid lines) and four TE525MM gauges (green dotted lines, averaged) in 3 rainfall events. (**a**) a rainfall event in spring, from 19–20 April 2019; (**b**) a rainfall event in summer, on 3 August 2019; (**c**) a rainfall event in autumn, on 1 September 2018.

The measuring range of Parsivel-2 is 0.25–6 mm, and it has been proved that the disdrometer has errors in measuring both smaller and larger diameters of raindrops in many studies [53,54], which have more accuracy in measuring mid-level raindrops in the spectra. Liu et al. [54] further explained the algorithm of the disdrometer and concluded that the differences can be attributed to a certain error of rainfall amount accumulation. In all three measured events, when the TE525MM Gauges-measured data reaches its peak (at 0:30 in (a), 19:00 in (b), and 18:30 in (c)), the data measured by gauges are all more than the disdrometer-measured data; and when the TE525MM Gauges-measured data reaches its minimum of the event (at 23:30 in (a), at 11:30 in (b) and 15:00 in (c)), the data measured by gauges are all no more than the disdrometer-measured data. As raindrop spectra data larger than 6 mm are treated as solid rainfall and eliminated, the peak value of the disdrometer is lessened. This is consistent with the results in Section 3.3 that in Event 1 the disdrometer- and gauge-measured $\overline{R}$ data indicates a significant gap (2.94 and 3.51 mm·h^{-1}, respectively). Since the measured raindrop spectra data larger than 6 mm have been removed, and raindrops of large diameter are often accompanied by heavy rain [25], it is speculated that this is the reason why the peak of rainfall intensity obtained by the raindrop disdrometer is smaller than the value measured by rain gauges.

4.2. Comparison of Different Z-R Relationships

In this section, the *Z*-*R* relationships of different experiment areas are compared, as shown in Table 3. The *Z*-*R* relationships calculated in different studies vary with different measurement methods, different study areas and rainfall time and types. Previous studies have shown that parameter a has a very wide range of values. This is consistent with Kang [55] that the range of parameter a is 10–1200. The parameters a and b vary with different seasons and locations, as well as with the measurement methods. It can be concluded that there is a great variation in the parameters a and b at different places, and *Z*-*R* relationships should be determined according to different regions. The above analysis also shows that it is of great significance to further improve the accuracy of radar rain measurement inversion and to further study the microphysical characteristics of rainfall [56].

Table 3. Results of *Z*-*R* relationships in different study areas.

Reference [57–62]	Precipitation Time/Season	Location	Measurement Method	*Z*-*R* relationships	Rainfall Type
Zhang et al., 1992	July in 1981	Jiangsu, Eastern China	Digital Radar	$Z = 60R^{2.3}$	Heavy rain
Marshall et al., 1947	Summer in 1946	Canada	MHF Radar	$Z = 190R^{1.72}$	Thunderstorm
Chen et al., 2008	15 July–7 August in 2007	Leizhou Peninsula, China	Parsivel Disdrometer	$Z = 269R^{1.54}$ $Z = 178R^{1.58}$	Convective rain Mixed-cloud rain
Marzuki et al., 2013	2006–2007	Kototabang, West Sumatra, Indonesia	2D-Video Disdrometer	$Z = 136R^{1.26}$	Stratiform rain
Hazenberg et al., 2011	14 September 2006	Cévennes-Vivarais region, France	OTT/Parsivel Disdrometer	$Z = 79R^{1.52}$	Stratiform rain
Blanchard, 1953	October in 1951–August in 1952	Hawaii, USA	Filter-paper	$Z = 31R^{1.71}$	Thunderstorm
Sivaramakrishnan, 1961	November in 1958	India	Filter-paper	$Z = 67.6R^{1.94}$	Thunderstorm

4.3. Sensitive Analysis of the Formula of KE-R Relationships

Many previous studies [22,52,63] have shown that parameters of the KE-*R* relationship are highly sensitive to DSD, and for parameters closely related to DSD characteristics, such as μ, the change in μ represents the difference in rainfall characteristics, which can affect the value of the parameters. Equation (18) indicates the KE-*R* relationships under the impact of parameter x. The parameter A and m are used to simplify the KE-*R* formula (expressed as Equation (18)) and are defined as:

$$A = \frac{\eta\Gamma(x)}{4.1^x} \tag{19}$$

$$\mathrm{m} = 0.21x \tag{20}$$

in which A and m are functions of parameter x, thus, A and m are affected by raindrop microphysical characteristics and the environmental conditions. The parameter x (known as a linear variation with the parameter μ according to the Equation (13)) varies differently due to the different regions, different time periods. Therefore, sensitivity analysis is conducted on the parameters A and m with the change of parameter x, in order to indicate the applicability of the KE-*R* relationships formula (derived as Equation (18)) under different rainfall conditions. S_1 and S_2 were defined as the parameters to analyze the sensitivity of A and m with the change of x, and the influence of change on parameter x on the KE-*R* relationships is further shown. The definition of sensitive parameters S_1 and S_2 are derived in Equations (21) and (22):

$$S_1 = \lim_{\Delta x \to 0}\left(\frac{\Delta A/A}{\Delta x/x}\right) = \frac{\mathrm{d}A}{\mathrm{d}x}\cdot\frac{x}{A} \tag{21}$$

$$S_2 = \lim_{\Delta x \to 0}\left(\frac{\Delta \mathrm{m}/\mathrm{m}}{\Delta x/x}\right) = \frac{\mathrm{dm}}{\mathrm{d}x}\cdot\frac{x}{\mathrm{m}} = 1 \tag{22}$$

in which S_1 (S_2) is the ratio of the change rate of parameter A (parameter m) to the change rate of parameter x. It is obvious from Equation (20) that the parameter m is proportional to parameter x, thus, S_2 is a constant, as shown in Equation (22). The sensitive parameter S_1 is further calculated of stratiform and convective rain obtained via disdrometer in different seasons, and the results are summarized in Table 4.

Table 4. Sensitive analysis results for parameter A with x of different precipitation types in different seasons and the total year.

	Spring	Summer	Autumn	Total Year
S_1(Stratiform)	4.10	4.68	3.83	4.29
S_1(Convective)	3.88	3.79	3.97	3.88

Table 4 shows the results of the sensitivity analysis for A with x of different precipitation types in different seasons. The sensitivity of parameter A varies with different precipitation types and seasons. In the whole-year scale, the S_1 is 4.29 of stratiform rain and 3.88 of convective rain, which indicates the parameter A of stratiform rain is more sensitive to the change of parameter x in the total year. The S_1 of stratiform rain in spring and summer is also more than that of convective rain in corresponding seasons. However, the S_1 of stratiform rain (3.83) is less than that of convective rain (3.97) in autumn, and the S_1 reaches its lowest in autumn among three seasons. The parameter x is affected by changes in environmental factors and rainfall types [64], and in autumn, the sensitivity of parameter A with the change of x is lower than in spring or summer. This explains the obvious decrease of parameter A in autumn compared with the other two seasons calculated in Section 3.4. For convective rain in different seasons, the S_1 from small to large is summer (3.79) < spring (3.88) < autumn (3.97).

According to Teng [65], the values of μ for raindrop spectra are between −1 and 4, and different μ values correspond to different rainfall characteristics. The larger the μ, the more likely it is to cause convective rain. In order to analyze the KE-R relationship when the rainfall shape parameter μ takes different values, the KE-R relationship curve of different values of μ was therefore made based on Equation (18), as shown in Figure 12a–f. The rule of this study is that both parameter A and m increase with the increase of μ. Figure 12g further shows the relationship among KE-R-μ. At a certain R, KE increases as μ increases. At the same rainfall intensity, the rainfall kinetic energy is also related to the rainfall type: the more the rainfall type is inclined to convective rain, the greater the rainfall kinetic energy will be, which can be explained by the Equation (18) and corresponds to the conclusions in other studies [66,67]. KE-R relationship changes with the change of the parameter x, according to Equation (18). From Equation (13), the parameter x can be calculated with a linear function from parameter μ. As discussed in Section 2.2, the parameter μ is correlated with the rainfall types; thus, the KE can be interpreted by the rainfall types according to Equation (18). In addition, different fitted formulas obtained in previous studies can be approximated with Equation (18) by changing the parameter μ (see Table A1), and the specific results can be approximated by Figure A1. This shows that the derived theoretical formula (Equation (18)) in this study is universal in various regions; however, whether the formula can be directly used to further analyze the KE-R relationship in other semi-arid areas should be further discussed in the future.

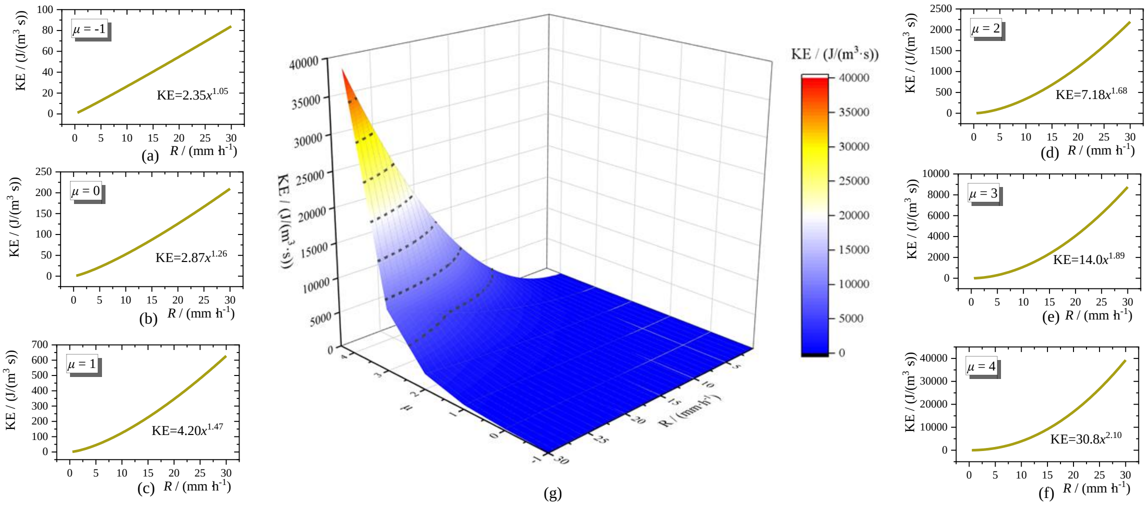

Figure 12. The *R*-KE relationships under different values of shape factors μ. The curves are derived based on Equation (18). (**a**) KE-*R* relationship for $\mu = -1$; (**b**) KE-*R* relationship for $\mu = 0$; (**c**) KE-*R* relationship for $\mu = 1$; (**d**) KE-*R* relationship for $\mu = 2$; (**e**) KE-*R* relationship for $\mu = 3$; (**f**) KE-*R* relationship for $\mu = 4$; (g) KE-*R*-μ relationship.

5. Conclusions

Characteristics of raindrop size distributions (DSDs) are important for improving the accuracy of radar reflectivity-rainfall intensity (*Z*-*R*) relationships in remote sensing (QPE) and the estimation of soil erosivity. In this study, an OTT Parsivel-2 Disdrometer is used to measured raindrop spectra from 10 August 2018 to 10 August 2019 in Yulin Ecohydrological Station, Shaanxi Province, China. The precipitation events obtained are classified as stratiform and convective rain based on the rainfall intensity classifying processes. The conclusions are summarized as follows.

(1) The characteristics of microphysical variables (the mass median diameter *Dm* and the raindrop size distribution *Nw*) were analyzed. The average *Dm* of different precipitation types in different seasons shows that for stratiform rain, rainfall intensity *R* is affected more by the average raindrop diameter *Dm*; for convective rain, *R* is affected more by DSD. The yearly average *Dm* and $\log_{10}Nw$ are 1.41 and 3.91 mm, respectively. The average *Dm* of stratiform (convective) rain from small to large is 1.38 mm (1.46 mm) in summer, 1.46 mm (1.52 mm) in spring and 1.51 mm (1.57 mm) in autumn. This reflects the semi-arid climate rainfall characteristics in Yulin Station.

(2) The variances of rainfall microphysical characteristics in different precipitation types and seasons are related. The distribution of rainfall terminal velocity-diameter (*v*-*D*) spectra of spring, summer and autumn is concentrated near the theoretical curve derived by Beard [45]. The base-10 logarithm of *Nw* is used to fit the relationship curves $\log_{10}Nw = \mathrm{c}R^{\mathrm{d}}$, in which c and d are parameters fitted by measured data. The difference in parameter d is small among different seasons (0.07–0.08 for stratiform rain and 0.02–0.04 for convective rain), and the d of stratiform rain is larger than that of convective rain.

(3) The *Z*-*R* relationships of different rainfall events in spring, summer and autumn in this semi-arid area are derived in this study. The parameter a is larger in stratiform rain than in convective rain, while the parameter b is larger in convective rain, showing the impact of different rainfall types on a and b. The results show that the estimation of different seasons should be treated, respectively.

(4) The theoretical formula of KE-*R* relationships for stratiform precipitation in semi-arid areas is derived ($\mathrm{KE} = \frac{\eta\Gamma(x)}{4.1^x}\cdot R^{0.21x}$, where the parameter η is constant and $x = \mu + 6.01$), which indicates the characteristics of precipitation and environmental conditions represented by parameter μ. This formula gives a general expression of the KE-*R* relationships and is simple to use because the parameters are all derived from the parameter μ. The sensitivity analysis results show that the parameter *A* for stratiform rain is more sensitive to the change of different precipitation types and environmental conditions in a

total year. The closer the precipitation types are to convective rain, the larger the KE is at the same level of R. By changing the parameter μ, different empirical formulas obtained in previous studies can be approximated with the derived theoretical formula (Equation (18)).

In summary, the DSD characteristics of Yulin Station were obtained and the results can help to understand the microphysical characteristics of precipitation and have a strong impact on the mechanism of soil erosivity in the semi-arid area. Additionally, the formula of KE-R relationships provides a convenient way to fit with different rainfall events in semi-arid areas by adjusting its parameters. But the results are not conclusive because of the limited sample records of different rainfall types. In this study, data in winter is not deeply investigated, e.g., the solid precipitation processes should be further considered and analyzed. Moreover, the impact of environmental conditions on the parameter A and m is still not well understood. In the future, the influence of environmental factors on the parameters in Z-R relationships should be further discussed.

Author Contributions: Conceptualization, Z.X.; Data curation, Z.X. and H.L.; Formal analysis, Z.X.; Funding acquisition, H.Y.; Methodology, Z.X. and H.Y.; Project administration, H.Y. and H.L.; Resources, H.L. and Q.H.; Supervision, H.Y.; Writing—original draft, Z.X.; Writing—review & editing, H.Y. All authors have read and agreed to the published version of the manuscript.

Funding: This research was partially supported by funding from the National Natural Science Foundation of China (Grant Nos. 51622903, 51979140 and 51809147), the National Program for Support of Top-notch Young Professionals, and the Program from the State Key Laboratory of Hydro-Science and Engineering of China (Grant No. 2017-KY-01). APC was funding by the National Natural Science Foundation of China (Grant No. 51622903).

Conflicts of Interest: The authors declare no conflict of interest.

Appendix A

Table A1 shows different fitting formulas of KE-R relationships in different research areas. KE-R formulas obtained in different regions vary, including polynomial, exponential, logarithm and other forms. In order to reflect the universality of the theoretical formulas introduced in this paper, KE-R relationships are obtained by changing equations based on Equation (18) to approximate the formulas given in different studies. The deterministic coefficient is used as the index to evaluate the approximation results, and the fitting results ensure that the deterministic coefficient of the two is greater than 0.99 for each reference listed in Table A1. The scatter points obtained by the KE-R relationship obtained by Equation (18) are described, and then, the linear fitting is performed with the points traced based on the original equation; results are shown in Figure A1. The abscissa is the KE obtained by changing different equations in this paper, and the ordinate is the relation obtained by different researchers. The red line is the fitting result. The rainfall intensity corresponding to the horizontal and vertical coordinates of each point on the line is the same. Figure A1 shows that the deterministic coefficients of different results are all above 0.99, indicating that Formula (18) can approximate the KE-R results obtained in different studies by changing the parameter values. Since the equation can be fixed only by determining the parameters, it has the value of further generalization.

Table A1. Different formulas of KE-R relationships.

References	KE-R Relationships (Originally Derived)	Form	KE-R Relationships (Based on Equation (18))	μ
Carter et al., 1974 [68]	$\mathrm{KE} = 11.32R + 0.5546R^2 - 0.5009 \times 10^{-2}R^3 + 0.126 \times 10^{-4}R^4$	Polynomial	$\mathrm{KE} = 4.38R^{1.49}$	1.09
McGregor et al., 1976 [69]	$\mathrm{KE} = R(27.3 + 21.68e^{-0.048R} - 41.26e^{-0.072R})$	Index	$\mathrm{KE} = 4.86R^{1.53}$	1.30
Wischmeier et al, 1978 [70]	$\mathrm{KE} = R(11.9 + 8.73\log R)$	Logarithm	$\mathrm{KE} = 4.62R^{1.51}$	1.20
Bollinne et al., 1984 [71]	$\mathrm{KE} = 12.32 \cdot R + 0.56 \cdot R^2$	Polynomial	$\mathrm{KE} = 4.79R^{1.53}$	1.27
Steiner et al., 2000 [67]	$\mathrm{KE} = 11R^{1.25}$	Power	$\mathrm{KE} = 4.86R^{1.53}$	1.30
Sanchez-Moreno et al., 2012 [72]	$\mathrm{KE} = (10.09 + 12\log R) \cdot R$	Logarithm	$\mathrm{KE} = 4.83R^{1.53}$	1.29

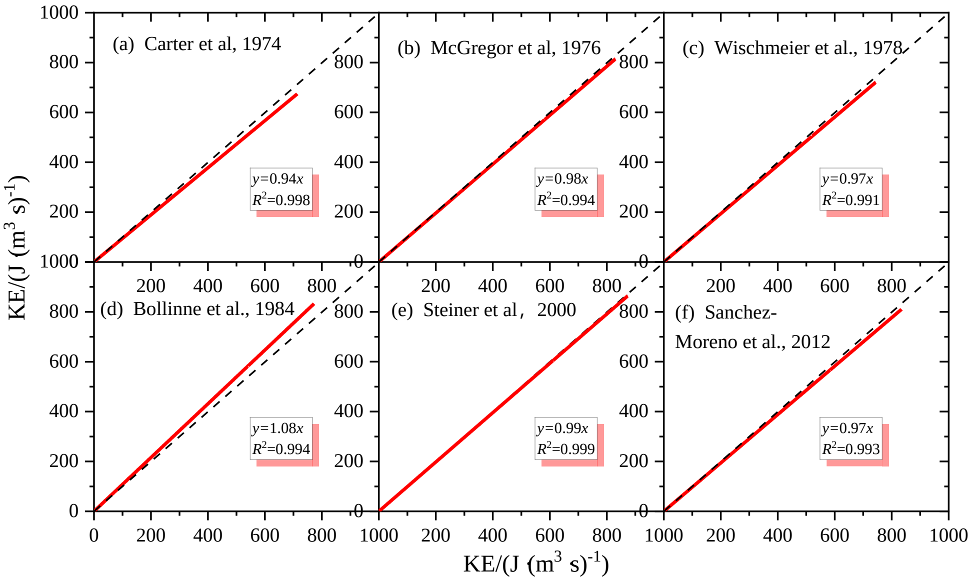

Figure A1. The approximated results of KE-*R* relationships derived by different studies are as follows: (**a**–**f**) are the linear relationships between KE-*R* obtained by this paper and KE-*R* obtained by different studies shown in Table A1, respectively.

References

1. Ding, B.; Yang, K.; Qin, J.; Wang, L.; Chen, Y.; He, X. The dependence of precipitation types on surface elevation and meteorological conditions and its parameterization. *J. Hydrol.* **2014**, *513*, 154–163. [CrossRef]
2. Chen, B.J.; Yang, J.; Pu, J.P. Statistical Characteristics of Raindrop Size Distribution in the Meiyu Season Observed in Eastern China. *J. Meteorol. Soc. Jpn.* **2013**, *91*, 215–227. [CrossRef]
3. Das, S.K.; Konwar, M.; Chakravarty, K.; Deshpande, S.M. Raindrop size distribution of different cloud types over the Western Ghats using simultaneous measurements from Micro-Rain Radar and disdrometer. *Atmos. Res.* **2017**, *186*, 72–82. [CrossRef]
4. Hazenberg, P.; Leijnse, H.; Uijlenhoet, R. The impact of reflectivity correction and accounting for raindrop size distribution variability to improve precipitation estimation by weather radar for an extreme low-land mesoscale convective system. *J. Hydrol.* **2014**, *519*, 3410–3425. [CrossRef]
5. Janapati, J.; Seela, B.K.; Reddy, M.V.; Reddy, K.K.; Lin, P.-L.; Rao, T.N.; Liu, C.-Y. A study on raindrop size distribution variability in before and after landfall precipitations of tropical cyclones observed over southern India. *J. Atmos. Sol.-Terr. Phys.* **2017**, *159*, 23–40. [CrossRef]
6. Hazenberg, P.; Yu, N.; Boudevillain, B.; Delrieu, G.; Uijlenhoet, R. Scaling of raindrop size distributions and classification of radar reflectivity–rain rate relations in intense Mediterranean precipitation. *J. Hydrol.* **2011**, *402*, 179–192. [CrossRef]
7. Waldvogel, A. TheN0Jump of Raindrop Spectra. *J. Atmos. Sci.* **1974**, *31*, 1067–1078. [CrossRef]
8. Schönhuber, M.; Randeu, W.L.; Baptista, J.P.V.P. Application of the 2D-video-distrometer for weather radar data inversion. *Phys. Chem. Earth Part B* **2000**, *25*, 1037–1042. [CrossRef]
9. Liu, X.; He, B.; Zhao, S.; Hu, S.; Liu, L. Comparative measurement of rainfall with a precipitation micro-physical characteristics sensor, a 2D video disdrometer, an OTT PARSIVEL disdrometer, and a rain gauge. *Atmos. Res.* **2019**, *229*, 100–114. [CrossRef]
10. Zhang, A.; Hu, J.; Chen, S.; Hu, D.; Liang, Z.; Huang, C.; Xiao, L.; Min, C.; Li, H. Statistical Characteristics of Raindrop Size Distribution in the Monsoon Season Observed in Southern China. *Remote Sens.* **2019**, *11*, 432. [CrossRef]
11. Raupach, T.H.; Berne, A. Correction of raindrop size distributions measured by Parsivel disdrometers, using a two-dimensional video disdrometer as a reference. *Atmos. Meas. Tech.* **2015**, *8*, 343–365. [CrossRef]
12. Bringi, V.N.; Chandrasekar, V.; Hubbert, J.; Gorgucci, E.; Randeu, W.L.; Schoenhuber, M. Raindrop size distribution in different climatic regimes from disdrometer and dual-polarized radar analysis. *J. Atmos. Sci.* **2003**, *60*, 354–365. [CrossRef]

13. Seliga, T.A.; Bringi, V.N. Potential use of the radar differential reflectivity measurements at orthogonal polarizations for measuring precipitation. *J. Appl. Meteorol.* **1976**, *15*, 69–76. [CrossRef]
14. Sulochana, Y.; Rao, T.N.; Sunilkumar, K.; Chandrika, P.; Raman, M.R.; Rao, S.V.B. On the seasonal variability of raindrop size distribution and associated variations in reflectivity—Rainrate relations at Tirupati, a tropical station. *J. Atmos. Sol.-Terr. Phys.* **2016**, *147*, 98–105. [CrossRef]
15. Wen, G.; Xiao, H.; Yang, H.L.; Bi, Y.H.; Xu, W.J. Characteristics of summer and winter precipitation over northern China. *Atmos. Res.* **2017**, *197*, 390–406. [CrossRef]
16. Carollo, F.G.; Ferro, V.; Serio, M.A. Predicting rainfall erosivity by momentum and kinetic energy in Mediterranean environment. *J. Hydrol.* **2018**, *560*, 173–183. [CrossRef]
17. Ji, L.; Chen, H.N.; Li, L.; Chen, B.J.; Xiao, X.; Chen, M.; Zhang, G.F. Raindrop Size Distributions and Rain Characteristics Observed by a PARSIVEL Disdrometer in Beijing, Northern China. *Remote Sens.* **2019**, *11*, 1479. [CrossRef]
18. Angulo-Martínez, M.; Barros, A.P. Measurement uncertainty in rainfall kinetic energy and intensity relationships for soil erosion studies: An evaluation using PARSIVEL disdrometers in the Southern Appalachian Mountains. *Geomorphology* **2015**, *228*, 28–40. [CrossRef]
19. Carollo, F.G.; Serio, M.A.; Ferro, V.; Cerdà, A. Characterizing rainfall erosivity by kinetic power - Median volume diameter relationship. *Catena* **2018**, *165*, 12–21. [CrossRef]
20. Meshesha, D.T.; Tsunekawa, A.; Tsubo, M.; Haregeweyn, N.; Tegegne, F. Evaluation of kinetic energy and erosivity potential of simulated rainfall using Laser Precipitation Monitor. *Catena* **2016**, *137*, 237–243. [CrossRef]
21. Abd Elbasit, M.A.M.; Yasuda, H.; Salmi, A.; Anyoji, H. Characterization of rainfall generated by dripper-type rainfall simulator using piezoelectric transducers and its impact on splash soil erosion. *Earth Surf. Process. Landf.* **2010**, *35*, 466–475. [CrossRef]
22. Serio, M.A.; Carollo, F.G.; Ferro, V. Raindrop size distribution and terminal velocity for rainfall erosivity studies. A review. *J. Hydrol.* **2019**, *576*, 210–228. [CrossRef]
23. Fan, Y.; Chen, Y.; Wei, J. An Analysis of Drought Features in Shaanxi Province. *J. Xi'an Univ. Technol.* **1996**, *12*, 200–206.
24. Li, Y.; Cao, Z.; Long, H.; Liu, Y.; Li, W. Dynamic analysis of ecological environment combined with land cover and NDVI changes and implications for sustainable urban–rural development: The case of Mu Us Sandy Land, China. *J. Clean. Prod.* **2017**, *142*, 697–715. [CrossRef]
25. Xie, Z.; Yang, H.; Lv, H. Study on the relationship between rainfall kinetic energy and rainfall intensity based on raindrop spectrum observations. *Water Resour. Hydropower Eng.* **2019**. under review.
26. Ulbrich, C.W. Natural Variations in the Analytical Form of the Raindrop Size Distribution. *J. Clim. Appl. Meteorol.* **1983**, *22*, 1764–1775. [CrossRef]
27. Testud, J.; Oury, S.; Black, R.A.; Amayenc, P.; Dou, X.K. The concept of "normalized" distribution to describe raindrop spectra: A tool for cloud physics and cloud remote sensing. *J. Appl. Meteorol.* **2001**, *40*, 1118–1140. [CrossRef]
28. Ulbrich, C.W.; Atlas, D. Rainfall microphysics and radar properties: Analysis methods for drop size spectra. *J. Appl. Meteorol.* **1998**, *37*, 912–923. [CrossRef]
29. Tokay, A.; Wolff, D.B.; Petersen, W.A. Evaluation of the New Version of the Laser-Optical Disdrometer, OTT Parsivel2. *J. Atmos. Ocean. Technol.* **2014**, *31*, 1276–1288. [CrossRef]
30. Zhang, H.; HE, H.; Zhang, Y.; Zeng, Q.; Bai, S. Parameter Characteristics Analysis of Raindrop Spectrum Fitting Models in Nanjing. *Meteorol. Environ. Sci.* **2017**, *40*, 77–84.
31. Seela, B.K.; Janapati, J.; Lin, P.L.; Wang, P.K.; Lee, M.T. Raindrop Size Distribution Characteristics of Summer and Winter Season Rainfall Over North Taiwan. *J. Geophys. Res.-Atmos.* **2018**, *123*, 11602–11624. [CrossRef]
32. Zhang, G.; Vivekanandan, J.; Brandes, E.A. The Shape–Slope Relation in Observed Gamma Raindrop Size Distributions: Statistical Error or Useful Information? *J. Atmos. Ocean. Technol.* **2003**, *20*, 1106–1119. [CrossRef]
33. Low, T.B.; List, R. Collision, Coalescence and Breakup of Raindrops. Part I: Experimentally Established Coalescence Efficiencies and Fragment Size Distributions in Breakup. *J. Atmos. Sci.* **1982**, *39*, 1591–1606. [CrossRef]
34. Tokay, A.; Bashor, P.G. An Experimental Study of Small-Scale Variability of Raindrop Size Distribution. *J. Appl. Meteorol. Clim.* **2010**, *49*, 2348–2365. [CrossRef]

35. Zhou, L.M.; Zhang, H.S.; Wang, J.; Wang, Q.; Chen, X.L. Raindrop Spectral Charcteristics of Mixed-cloud Precipitation in Shandong Province. *Meteorol. Sci. Technol.* **2010**, *38*, 73–77.
36. Li, H.; Yin, Y.; Shan, Y.; Jin, Q. Statistical Characteristics of Raindrop Size Distribution for Stratiform and Convective Precipitation at Different Altitudes in Mt. Huangshan. *Chin. J. Atmos. Sci.* **2018**, *42*, 268–280.
37. Chen, C.; Yin, Y.; Chen, B.J. Raindrop Size Distribution at Different Altitudes in Mt. Huang. *Trans. Atmos. Sci.* **2015**, *38*, 388–395. [CrossRef]
38. Kinnell, P. Rainfall Intensity-Kinetic Energy Relationships for Soil Loss Prediction 1. *Soil Sci. Soc. Am. J.* **1981**, *45*, 153–155. [CrossRef]
39. Atlas, D.; Ulbrich, C.W. Path-and area-integrated rainfall measurement by microwave attenuation in the 1–3 cm band. *J. Appl. Meteorol.* **1977**, *16*, 1322–1331. [CrossRef]
40. Marshall, J.S.; Palmer, W.M.K. The Distribution of Raindrops with Size. *J. Meteorol.* **1948**, *5*, 165–166. [CrossRef]
41. Uijlenhoet, R.; Stricker, J. A consistent rainfall parameterization based on the exponential raindrop size distribution. *J. Hydrol.* **1999**, *218*, 101–127. [CrossRef]
42. Lane, J.; Hackathorn, M.; Kewley, J.; Madore, M.; May, M.; Briggs, C.; DeLeon Springs, F. A method for estimating 3-D spatial variations of rainfall drop size distributions over remote ocean areas. Presented at the Fifth International Conference on Remote Sensing for Marine and Coastal Environments, San Diego, CA, USA, 5–7 October 1998; p. 7.
43. Ochou, A.D.; Nzeukou, A.; Sauvageot, H. Parametrization of drop size distribution with rain rate. *Atmos. Res.* **2007**, *84*, 58–66. [CrossRef]
44. Li, P.; Sun, X.; Zhao, X. Analysis of precipitation and potential evapotranspiration in arid and semi-arid area of China in recent 50 years. *J. Arid Land Res. Environ.* **2012**, *7*, 57–63.
45. Beard, K.V. Terminal Velocity and Shape of Cloud and Precipitation Drops Aloft. *J. Atmos. Sci.* **1976**, *33*, 851–864. [CrossRef]
46. Hunt, W.F.; Jarrett, A.R.; Smith, J.T.; Sharkey, L.J. Evaluating bioretention hydrology and nutrient removal at three field sites in North Carolina. *J. Irrig. Drain. Eng.* **2006**, *132*, 600–608. [CrossRef]
47. Hunter, S.M. WSR-88D radar rainfall estimation: Capabilities, limitations and potential improvements. *Natl. Weather Dig.* **1996**, *20*, 26–38.
48. Austin, P.M. Relation between Measured Radar Reflectivity and Surface Rainfall. *Mon. Weather Rev.* **1987**, *115*, 1053–1071. [CrossRef]
49. Sauvageot, H. Rainfall Measurement by Radar—A Review. *Atmos. Res.* **1994**, *35*, 27–54. [CrossRef]
50. Wilson, J.W.; Brandes, E.A. Radar measurement of rainfall—A summary. *Bull. Am. Meteorol. Soc.* **1979**, *60*, 1048–1060. [CrossRef]
51. Zhang, P.; Du, B.; Dai, T.P. *Radar Meteorology*; China Meteorological Press: Beijing, China, 2001.
52. Petan, S.; Rusjan, S.; Vidmar, A.; Mikos, M. The rainfall kinetic energy-intensity relationship for rainfall erosivity estimation in the mediterranean part of Slovenia. *J. Hydrol.* **2010**, *391*, 314–321. [CrossRef]
53. Battaglia, A.; Rustemeier, E.; Tokay, A.; Blahak, U.; Simmer, C. PARSIVEL Snow Observations: A Critical Assessment. *J. Atmos. Ocean. Technol.* **2010**, *27*, 333–344. [CrossRef]
54. Liu, X.C.; Gao, T.C.; Liu, L. A comparison of rainfall measurements from multiple instruments. *Atmos. Meas. Tech.* **2013**, *6*, 1585–1595. [CrossRef]
55. Kang, L. *A Study on Dynamic Correction for Radar-Derived Quantitation Precipitation Estimation Based on the Optimal Z-I Relationship*; Lanzhou University: Lanzhou, China, 2014.
56. Yuan, X.; Ni, G.; Pan, A.; Wei, L. NEXRAD Z-R Power Relationship in Beijing Based on Optimization Algorithm. *J. Chin. Hydrol.* **2010**, *30*, 1–6.
57. Zhang, P.; Dai, T.; WANG, D.; Lin, B. Derivation of The Z-I Relationship by Optimization and The Accuracy in The Quantitative Rainfall Measurement. *Sci. Meteorol. Sin.* **1992**, *12*, 333–338.
58. Marshall, J.S.; Langille, R.C.; Palmer, W.M.K. Measurement of Rainfall by Radar. *J. Meteorol.* **1947**, *4*, 186–192. [CrossRef]
59. Chen, Q.; Niu, S.; Zhang, Y.; Xu, F. Z-R Relationship from the Particle Size and Velocity (Parsivel) optical disdrometer and its Application in Estimating Areal Rainfall. In Proceedings of the 2008 2nd International Conference on Bioinformatics and Biomedical Engineering, Shanghai, China, 16–18 May 2008.

60. Marzuki; Randeu, W.L.; Kozu, T.; Shimomai, T.; Hashiguchi, H.; Schönhuber, M. Raindrop axis ratios, fall velocities and size distribution over Sumatra from 2D-Video Disdrometer measurement. *Atmos. Res.* **2013**, *119*, 23–37. [CrossRef]
61. Blanchard, D.C. Raindrop Size-Distribution in Hawaiian Rains. *J. Meteorol.* **1953**, *10*, 457–473. [CrossRef]
62. Sivaramakrishnan, M.V. Studies of raindrop size characteristics in different types of tropical rain using a simple recorder. *Indian J. Meteorol. Geophys.* **1961**, *12*, 189–217.
63. Yakubu, M.L.; Yusop, Z.; Fulazzaky, M.A. The influence of rain intensity on raindrop diameter and the kinetics of tropical rainfall: Case study of Skudai, Malaysia. *Hydrolog. Sci. J.* **2016**, *61*, 944–951. [CrossRef]
64. Takeuchi, D. Characterization of raindrop size distributions. In Proceedings of the Conference on Cloud Physics and Atmospheric Electricity, Issaquah, WA, USA, 31 July–4 August 1978; pp. 154–161.
65. Teng, X. *Sensitivity of the W Band Airborne Cloud Radar Reflectivity Factor Z to Cloud Parameters*; Nanjing University of Information Science and Technology: Nanjing, China, 2011.
66. Park, S.W.; Mitchell, J.K.; Bubenzer, G.D. An analysis of splash erosion mechanics. In Proceedings of the ASAE 1980 Winter Meeting, Chicago, IL, USA, 4 December 1980; p. 27.
67. Steiner, M.; Smith, J.A. Reflectivity, rain rate, and kinetic energy flux relationships based on raindrop spectra. *J. Appl. Meteorol.* **2000**, *39*, 1923–1940. [CrossRef]
68. Carter, C.E.; Greer, J.D.; Braud, H.J.; Floyd, J.M. Raindrop Characteristics in South Central United-States. *Trans. ASAE* **1974**, *17*, 1033–1037. [CrossRef]
69. McGregor, K.C.; Mutchler, C.K. Status of the R factor in northern Mississippi. In *Soil Erosion: Prediction and Control, Soil Conservation Soc. Amer.*; Nature: UK, 1976; pp. 135–142.
70. Wischmeier, W.H.; Smith, D.D. *Predicting Rainfall Erosion Losses: A Guide to Conservation Planning*; Science and Education Administration, US Department of Agriculture: Washington, WA, USA, 1978; Volume 537.
71. Bollinne, A.; Florins, P.; Hecq, P.; Homerin, D.; Renard, V. Etude de l'énergie des pluies en climat tempéré océanique d'Europe Atlantique. *Zeitschrift für Geomorphologie* **1984**, *49*, 27–35.
72. Sanchez-Moreno, J.F.; Mannaerts, C.M.; Jetten, V.; Loffler-Mang, M. Rainfall kinetic energy-intensity and rainfall momentum-intensity relationships for Cape Verde. *J. Hydrol.* **2012**, *454*, 131–140. [CrossRef]